Silicon ring resonator-coupled Mach-Zehnder interferometers for the Fano resonance in the mid-IR

Benedetto Troia,[1,2,*] Jordi Soler Penades,[3] Zhibo Qu,[3] Ali Z. Khokhar,[3] Ahmed Osman,[3] Yangbo Wu,[3] Callum Stirling,[3] Milos Nedeljkovic,[3] Vittorio M. N. Passaro,[2] and Goran Z. Mashanovich,[3]

[1]*Currently at imec, Kapeldreef 75, 3001 Heverlee, Belgium*
[2]*Department of Electrical and Information Engineering, Politecnico di Bari, Via E. Orabona 4, 70125 Bari, Italy*
[3]*Optoelectronics Research Centre, University of Southampton, Southampton SO17 1BJ, UK*
**Corresponding author: dr.benedetto.troia@gmail.com*

Received XX Month XXXX; revised XX Month, XXXX; accepted XX Month XXXX; posted XX Month XXXX (Doc. ID XXXXX); published XX Month XXXX

We present ring resonator-coupled Mach-Zehnder interferometers (MZI) based on silicon-on-insulator (SOI) rib waveguides, operating around the mid-IR wavelength of 3.8 μm. A number of different photonic integrated devices have been designed and fabricated experimentally to obtain the asymmetric Fano resonances in the mid-IR. We have investigated the influence of the coupling efficiency between the ring resonator (RR) and the MZI as well as the phase shift between the two arms of the MZI on the Fano-type resonance spectral features in agreement with theoretical predictions. Finally, wavelength-dependent Fano transmittances have been successfully measured with insertion losses up to ~1 dB and extinction ratios of ~20 dB. A slope of sharp Fano resonances as high as -547.6/μm has been achieved and estimated to be 35.5 % higher than the slope of single ring resonator Lorentzian-type resonances.

OCIS codes: (130.3120) Integrated optics devices; (130.3060) infrared; (230.1150) all-optical devices.

http://dx.doi.org/10.1364/AO.99.099999

1. INTRODUCTION

In recent years, the mid-IR wavelength range has become a very attractive and promising spectral region to be explored for a wide range of applications, such as environmental and biochemical-sensing, defence, security, communications, and astronomy, to name a few [1]. In this context, research effort has been carried out in order to extend the operation of silicon photonic devices from the near-infrared to the mid-IR wavelength range. Actually, several results on state-of-the-art mid-IR lasers and photodetectors have been recently reported in the literature [2-4] as well as passive and active photonic integrated devices successfully demonstrated, i.e. multimode interferometers, ring resonator, MZIs, spectrometers, modulators, multiplexers and (de)multiplexers, fabricated on silicon and germanium technology platforms and operating at wavelengths up to ~ 7.5 μm [5-13].

In this context, it is worth emphasizing the need of further extending the library of active and passive mid-IR photonic devices, especially operating in the short-wave spectral range (2-4 μm), where several molecules exhibit strong absorption and can be efficiently detected, paving the way to high-performance photonic sensing applications. Furthermore, this wavelength region has emerged as a very suitable candidate for optical communication systems due to the increasing internet traffic and consequent growing bandwidth demand.

A combination of photonic devices, such as a ring resonator and an MZI, can be designed to exhibit special wavelength-dependent transmittances that can be useful to enhance the performance of photonic sensors and filters. In this context, Fano-type resonances have been widely investigated in the literature due to very sharp and asymmetrical shapes and potential application in high-performance sensing, optical filtering and switching applications [14]. In particular, Fano resonances result from the interference between a resonance pathway and a coherent background pathway. Moreover, they can be varied by tuning the relative phase between the resonances and coherent background pathways, and are ubiquitous in a large number of optical resonant configurations and nanophotonics devices [15-17], including, for example, integrated nested ring resonator, standard ring resonator and multiple ring resonators loaded on an MZI arms, as well as exotic photonic integrated architectures [18-33]. Finally, it has been demonstrated that RR-coupled MZI devices can exhibit a 30.5% enhancement in sensitivity over conventional ring resonators [22], making them suitable for photonic sensing and filtering.

Recently, a few experimental investigations have been performed to obtain Fano resonances in the mid-IR. In particular, encouraging results have been demonstrated in photonic crystal membranes [34], heavily doped silicon and metallic nanostructures [35], graphene hybrid waveguide structures [36], semiconductor dielectric resonators

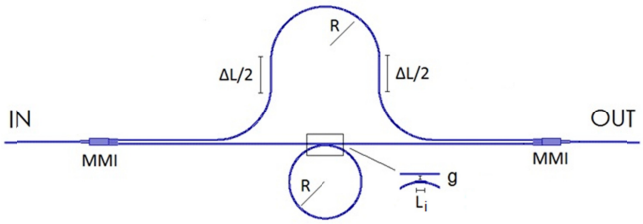

Fig. 1. Schematic of a RR-coupled MZI device. Input/output waveguides and multimode interferometers (MMIs), the MZI phase shift geometrical parameter ΔL, the RR radius, R, the directional coupler gap, g, and interaction length, L_i, are labeled in.

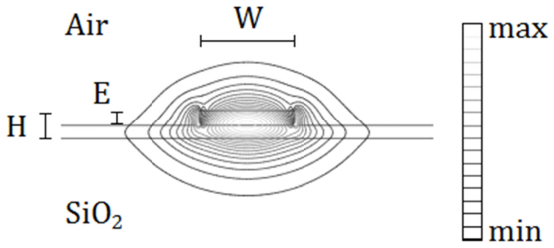

Fig. 2. The spatial distribution of the E_x component of the quasi-TE polarized fundamental optical mode (TE_{00}) with nominal waveguide dimensions (W = 1350 nm, H = 400 nm, and E = 220 nm) at the wavelength of λ = 3.75 μm.

made of cylinder arrays [37], and in a RR with an interferometric waveguide-based architecture [38].

In this paper, we demonstrate for the first time to the best of our knowledge, asymmetric Fano-type resonances in CMOS-compatible photonic RR-coupled MZIs based on integrated silicon-on-insulator rib waveguides operating around 3.8 μm. In particular, we designed and fabricated a number of integrated architectures for investigating the influence of the coupling efficiency between the ring resonator and the MZI as well as the phase shift between the two MZI arms on the Fano resonance shape and spectral features. Detailed design guidelines are reported to allow the device and performance to be reproducible in a CMOS-compatible foundry. Moreover, the technology platform used in this investigation is characterized by a 400 nm-thick silicon layer that is also suitable for the fabrication of ultra-compact photonic integrated circuits operating in the near-IR, at telecom wavelengths around 1.55 μm [5]. In this way, near-IR and mid-IR silicon photonic devices can be fabricated on the same standard platform by means of optimal fabrication processes and recipes. Rigorous experimental analysis reveal information about the suitable range of directional coupler gaps to achieve asymmetric Fano-type resonances with a good agreement with simulation results. Finally, we elucidate on potential applications of such devices in optical filtering, switching and sensing, and provide rigorous methodology and design criteria for enhancing the overall Fano sensitivity.

2. DESIGN AND FABRICATION

A sketch of a representative photonic integrated Fano device is shown in Fig. 1. The architecture is characterized by an input 3-dB splitter and an output combiner using 1×2 multimode interferometers [39]. In addition, the ring resonator radius, R, the gap of the directional coupler, g, as well as the straight waveguide paths of the upper arm of the MZI i.e., $\Delta L/2$, have also been labeled in.

The design and operation principle of the Fano devices proposed in this paper have been widely investigated and reported in the literature so far [18-33]. Actually, by loading one arm of the MZI with a ring resonator, the amplitude and phase of typical wavelength-dependent cos^2 MZI transmittances can be dramatically modified. This behavior is mainly dependent on the coupling efficiency between the ring and the MZI, and, specifically, on the power coupling coefficients of the directional couplers that depend on the coupler gap, g, and interaction length, L_i, as sketched in Fig. 1. In particular, the higher the coupling efficiency the stronger the influence of the ring resonator on typical MZI operation. In fact, when a tunable laser source is used to characterize a RR-coupled MZI architecture, the emitted wavelengths that correspond to the ring resonator resonances are filtered in the bottom arm and transmitted to the 3-dB combiner at the output with a phase shift of 2π and an amplitude that depends on the extinction ratios of the ring resonator [40]. Conversely, those signals propagating in the ring resonator all-pass bands are transmitted with an amplitude and phase that depend on the ring resonator insertion losses and the MZI lower arm length (Fig. 1), respectively.

Design criteria can be elucidated by referring to the signal phase of the MZI reference arm (the upper arm in Fig. 1), Φ_{ref}, and the power coupling coefficient of the directional coupler, κ_c^2. In particular, the normalized sensitivity of the RR-coupled MZI device, $S_{Fano,norm}$, can be written as in Eq. (1) [22].

$$S_{Fano,norm} = (\kappa_{c,crit}^2 S_{Fano})/P_{in} \quad (1)$$

In Eq. (1), P_{in} is the input optical power, S_{Fano} is the slope of the asymmetric Fano resonance, thus the first order derivative of the output optical power, P_{out}, with respect to the ring resonator round-trip phase, $\Phi_{RR} = (4\pi^2 R n_{eff})/\lambda$, where n_{eff} is the waveguide effective index and λ is the operating wavelength. Furthermore, $\kappa_{c,crit}^2 = 2\pi R\alpha$ is the critical power coupling coefficient of the ring resonator [40], with α being the waveguide propagation loss. Finally, a normalized power coupling coefficient can be defined as $\kappa_{c,norm}^2 = \kappa_c^2/\kappa_{c,crit}^2$, where κ_c^2 is the power coupling coefficient of the ring resonator with values in the range from 0 to 1. In this way, a relationship between κ_c^2 and the Fano sensitivity is determined. In particular, M. Terrel et al. performed a numerical analysis of Eq. (1) and demonstrated that the best performance of the RR-coupled MZI Fano device can be achieved when the ring resonator operates in critical coupling, i.e., $\kappa_c^2 = \kappa_{c,crit}^2$, and the signal phase of the MZI reference arm, Φ_{ref}, is equal to π/2, provided that input and output 3-dB splitter and combiner are used, respectively [22].

The devices reported in this paper are based on SOI rib waveguides with height H = 400 nm, width W = 1350 nm, and etch depth E = 220 nm, and 2000 nm of buried oxide, resulting in single mode propagation of the fundamental quasi-TE (i.e., transverse electric) polarized optical mode. A cross-sectional view of the waveguide is plotted in Fig. 2, where the spatial distribution of the E_x component of the quasi-TE polarized fundamental optical mode (TE_{00}) is simulated with nominal waveguide dimensions at the wavelength of 3.75 μm. It is worth specifying that, despite the high silicon dioxide absorption around the wavelength of 3.8 μm (~ 5-6 dB/cm [41]), record low loss of 1.46 ± 0.20 dB/cm has been demonstrated by the authors in rib waveguides operating at 3.8 μm (Fig. 2) [39]. In fact, such a result was achieved by

performing an optimal design of the waveguide structures in order to minimize the optical confinement of the fundamental mode in the buried silicon dioxide (SiO_2). Moreover, state-of-the-art processing facilities and optimized recipes facilitated the fabrication of high-quality devices with low loss. In particular, the rib waveguide patterns were written using a JEOL JBX 9300FS e-beam lithography tool on 6-inch SOI wafer. A non-chemically amplified high resolution positive resist (i.e., ZEP-520A) from Nippon Zeon was used, and patterns in ZEP-520A were transferred to the SOI wafers by inductively coupled plasma etching (ICP), using an Oxford Instrument ICP 380 plasma system.

A theoretical and experimental investigation of SOI ring and racetrack resonators based on the aforementioned rib waveguides and operating around a mid-IR wavelength of 3.8 μm is reported in [7]. In particular, it is worth specifying that different resonators were demonstrated exhibiting insertion loss less than 1 dB, quality factor up to 3,000, and extinction ratios up to ~ 30 dB. Furthermore, an in-depth experimental analysis of bending losses in such devices was carried out, demonstrating that a radius as short as 20 μm introduces bending losses of 0.073 ± 0.003 dB/90°, while doubling the radius up to 40 μm losses decrease at a value of 0.033 ± 0.003 dB/90°. As a result, the bending radius used in the RR-coupled MZI architectures proposed in this paper is R = 60 μm so that negligible bending loss can be assumed in the design procedures as well as in real device operation.

We have implemented a rigorous mathematical modelling based on the scattering matrix method for the simulation and design of different Fano device configurations [22]. In fact, the design of guided-wave directional couplers was performed using a sophisticated modelling already developed and successfully demonstrated in [42]. Finally, fabrication tolerances of ± 20 nm for the waveguide width, W, and etch depth, E, were taken into account, and chromatic dispersion in the 3.7-3.9 μm wavelength range was included in the simulations by means of silicon and silicon dioxide conventional Sellmeier equations.

Two Fano RR-coupled MZI device configurations, namely Fano #A and Fano #B, were designed and fabricated and their geometrical parameters are listed in Table 1. In particular, #A and #B Fano architectures are characterized by the same ring resonator radius of 60 μm and a directional coupler gap, g, which was varied from minimum values of 300 nm (Fano #A) and 400 nm (Fano #B) to a maximum of > 1000 nm, namely ∞, which is practically equivalent to a coupling efficiency equal to zero. In addition, the interaction length of the directional couplers was designed to be 0 μm in Fano #A devices, thus determining a point coupling between the ring resonator and the MZI arm. Conversely, a length of L_i = 5 μm was designed in Fano #B devices, resulting in different coupling efficiencies compared to Fano #A architectures. Finally, referring to Fig. 1, it is worth specifying that the ring radius, R, also characterizes the bend waveguides in the upper arm of the MZI. Furthermore, the difference between the overall path lengths of the bottom arm without the ring resonator and the upper arm of the MZI is defined as $\Delta L + 2R(\pi - 2)$. Consequently, as the parameter R is fixed at the value of 60 μm in both Fano #A and Fano #B configurations, the phase difference between the signals propagating in the upper and lower MZI arms can be set by properly designing the parameter ΔL. In particular, values of $\Delta L = 50$ μm (Fano #A) and $\Delta L = 0$ μm (Fano #B) were selected to tune the reference signal phases in the upper MZI arm in the range $|\Phi_{ref}| = [\frac{\pi}{4}, \frac{\pi}{2}]$, where $|\Phi_{ref}| = \pi/2$ corresponds to the optimal condition for achieving the best Fano sensitivity [22]. It is worth noting that predictions of Φ_{ref} are difficult because experimental signal phase contributions strongly depend on the effective index of the fabricated structures, thus on the process variability of the foundry's fabrication conditions. Finally, the parameter ΔL also affects the free spectral range of the Mach-Zehnder interferometer when the ring resonator is not loaded i.e., when the coupling efficiency tends to zero. As a consequence, we selected two values of ΔL also to achieve different MZI free spectral ranges in Fano #A and Fano #B devices, respectively.

Table 1. Geometrical parameters of Fano #A and Fano #B architectures.

Parameters	Fano #A	Fano #B
ΔL (μm)	50	0
R (μm)	60	60
L_i (μm)	0	5
g(nm)	[400-∞]	[300-∞]

3. RESULTS AND DISCUSSION

The mid-IR experimental setup described in [43] was used for the characterization of the devices reported here. In particular, the light was coupled by means of input and output grating couplers specifically designed for coupling TE polarized optical signal. A tunable quantum cascade laser emitting at wavelengths in the range of 3.7-3.9 μm was tuned with a spectral sampling step of 0.02 nm for experimental data acquisition. The quantum cascade laser operates at wavelengths in the range of 3.72-3.90 μm, in either continuous wave or pulsed modes. The laser temperature was maintained at 21°C by using a chiller. The maximum continuous wave optical output power of the laser is ~150 mW at its peak wavelength of 3.80 μm. The nominal tuning accuracy is ± 0.5 cm^{-1} (± 1.9 nm at λ = 3.8 μm), and the nominal linewidth is ± 0.003 cm^{-1} (± 11 pm at λ = 3.8 μm). Finally, the laser is not mode-hop free as it manifests a significant jitter of the laser wavelength which is approximately ± 1 nm. Experimental results of Fano #A and Fano #B devices are plotted in Fig. 3 and Fig. 4, respectively.

In Figs. 3(a)-3(f), normalized measured transmittances of Fano #A devices are plotted in an arbitrary unit (a. u.) scale as a function of different directional coupler gaps. Furthermore, the corresponding theoretical spectra calculated by means of our implemented modelling are also shown. It is worth specifying that a propagation loss coefficient of α = 2 dB/cm was used in simulations [39] and a group index of n_g = 3.6533 corresponding to the waveguide nominal dimensions, was varied according to the waveguide fabrication tolerances of ± 20 nm in order to fit the experiments. Actually, spectral positions of the Fano transmittance discontinuities were estimated in good agreement with theory, while the amplitude values and shapes were not always perfectly matched with measurements. This is due to the fact that slightly varying values of α and power coupling coefficients, κ_c^2, across the chip can determine ring resonator dips with different extinction ratios and linewidths, thus affecting the Fano spectral features at the output. Finally, the maximum values of the calculated transmittances in Figs. 3(a)-3(f) are equal to 1 arbitrary unit because insertion losses were intentionally not included in the simulations. The reasons of this are the following: i) we were mainly interested in estimating the spectral positions and shapes of the Fano transmittance discontinuities as a function of directional coupler gaps, ii) the normalization of RR-coupled MZI device spectra with reference straight waveguide transmittances resulted in insertion losses that were not uniformly distributed throughout the wavelength range of ~ 3.72-3.86 μm due to slightly different input/output grating behaviour as shown in Fig. 3(f). It is worth specifying that the aforementioned insertion loss is the loss of the Fano device when it is inserted in the circuit and, because of the normalization with the reference straight waveguide transmittance, it does not include experimental setup loss, input-output coupling loss, and access waveguide loss.

Figures 3(a)-3(f) refer to directional coupler gaps equal to 400 nm, 500 nm, 600 nm, 700 nm, 800 nm, and ∞, corresponding to estimated

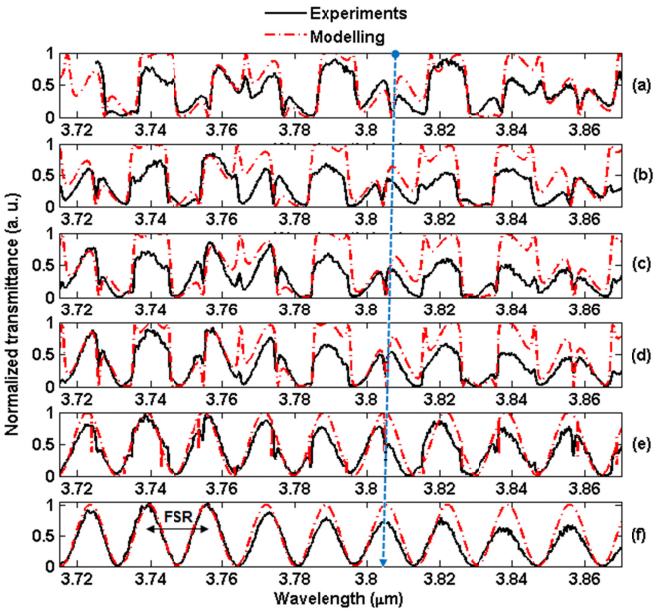

Fig. 3. Theoretical and experimental spectra of Fano #A device in a broad spectral range. Fano transmittances are plotted as a function of different values of the directional coupler gap: (a) g = 400 nm, (b) g = 500 nm, (c) g = 600 nm, (d) g = 700 nm, (e) g = 800 nm, (f) $g = \infty$. The MZI free spectral range (FSR) is indicated in Figure 3(f). The dashed arrow indicates the misalignment among the spectra.

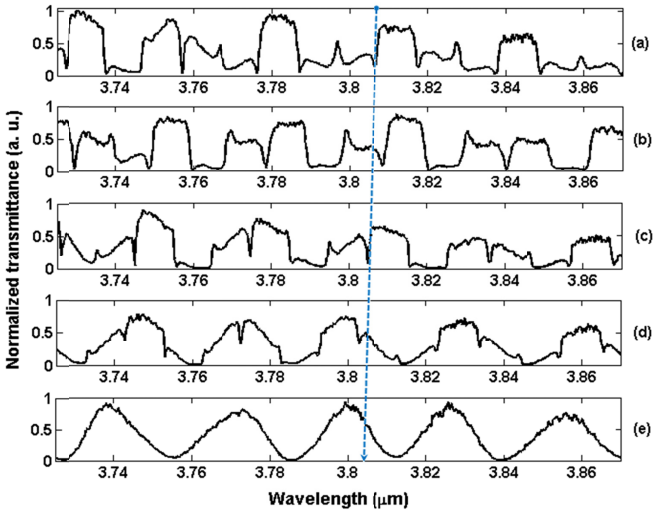

Fig. 4. Experimental spectra of Fano #B device in a broad spectral range. Fano transmittances are plotted as a function of different values of the directional coupler gap: (a) g = 300 nm, (b) g = 400 nm, (c) g = 700 nm, (d) g = 800 nm, (e) $g = \infty$. The dashed arrow indicates the misalignment among the spectra.

power coupling coefficients, κ_c^2, equal to 0.36, 0.24, 0.15, 0.10, 0.06, and 0, respectively.

Experimental results confirm that Fano-type asymmetric line-shapes have been successfully achieved and the expected device operation as a function of the coupling efficiency has also been demonstrated. In particular, it is evident that when the coupling efficiency between the ring resonator and the upper MZI arm is strong, (i.e., power coupling coefficient $\kappa_c^2 > 0.1$, thus $g < 700$ nm) typical asymmetric non-uniformities characterize the Fano transmittance and strongly depend on the phase shifts of the optical signals that interfere at the output combiner. This behavior can be observed in Figs. 3(a)-3(c). Conversely, when the coupling efficiency is low (i.e., $\kappa_c^2 < 0.1$, thus $g \geq 700$ nm) the influence of the ring resonator on the MZI operation is not optimal for generating the asymmetric Fano transmittance shapes as also plotted in Figs. 3(d)-3(e). Indeed, the typical periodic lobe distribution of the MZI transmittance can be clearly distinguished in Fig. 3(e), thus demonstrating that the Fano #A device is not properly operating for exhibiting the desired Fano resonances. Furthermore, it can be noticed that the experimental Fano #A transmittance in Fig. 3(e) is characterized by several dips that correspond to the ring resonator resonant wavelengths. This behavior demonstrates that phase-shift dependent Fano non-uniformities are not generated with a directional coupler gap of 800 nm, confirming that the upper limit for g is 700 nm in the Fano #A configuration. It is worth specifying that the variation of the Fano transmittance shape is particularly large as a function of the directional coupler gap g at values that are close to the upper limit. Consequently, a smaller step of the directional coupler gap variation, e.g., < 50 nm instead of 100 nm, would allow this physical behavior to be better observed experimentally. However, this is not the main scope of this investigation as we are interested mainly in the device operation when strong coupling efficiency occurs. Finally, the changes of the Fano transmittance for g values that are close to the upper limit can be clearly observed in the experimental spectra of the Fano #B devices plotted in Figs. 4(a)-4(e).

A MZI free spectral range equal to ~ 16 nm can be easily measured in Fig. 3(f) when the coupling efficiency between the ring resonator and the MZI is zero and the unperturbed MZI transmittance is achieved at the output. To this purpose, it is worth specifying that the FSR of the loaded ring resonator is shorter than the MZI free spectral range and it is equal to ~10 nm. Generally, the free spectral range of the perturbing photonic devices, i.e., the ring resonator, should be shorter than that of the MZI. Indeed, if this condition is not satisfied, the efficiency of the device is dramatically decreased because the asymmetric Fano resonances are not generated in the spectral window where no ring resonator resonances are located. Finally, it is worth noting that the experimental RR-coupled MZI transmittances plotted in Figs. 3(a)-3(f) as a function of different directional coupler gaps are almost aligned to each other, demonstrating an accurate control and reliability of the fabrication processes. Similarly, this feature is observed in Figs. 4(a)-4(e) although larger misalignments occurred as a result of process variability throughout the 6-inch SOI wafer. Nevertheless, waveguide fabrication tolerances were within the range of ± 20 nm.

Fano #B devices exhibited a similar behavior compared to Fano #A RR-coupled MZIs as also demonstrated by the experimental spectra plotted in Figs. 4(a)-4(e). In fact, these configurations are characterized by $\Delta L = 0$, then the difference between the overall path lengths of the bottom arm without the ring resonator and the upper arm of the MZI is $2R(\pi - 2) = 137$ μm (in Fano #A configuration it is 50 μm longer, i.e., 187 μm). As a consequence, the free spectral range of the Fano #B MZI with a directional coupler gap, $g = \infty$, thus $\kappa_c^2 = 0$, is expected to be larger than 16 nm. As a demonstration of this, the free spectral range measured experimentally in Fig. 4(e) is ~ 27 nm, thus approximately 10 nm larger compared to the previous configuration and still larger than the free spectral range of the loaded ring resonator.

It is worth noting that the Fano spectra plotted in Fig. 3 and Fig. 4 and measured by those devices characterized by a strong coupling efficiency, exhibit flat-bands span that we believe can be useful for

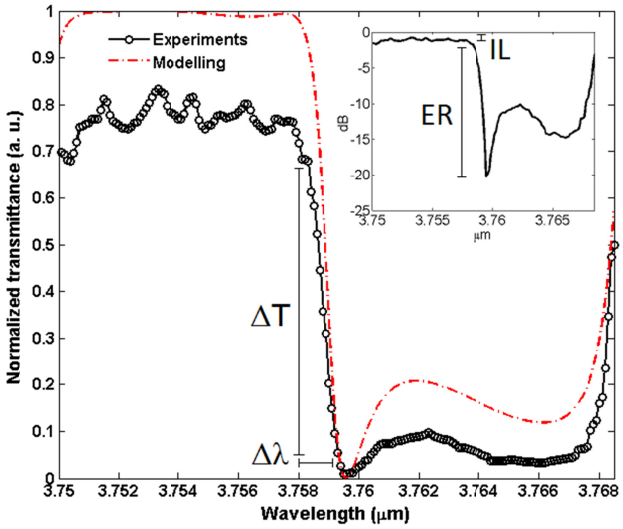

Fig. 5. Zoomed theoretical and experimental spectra of the Fano #B device with a directional coupler gap of g = 400 nm plotted in the wavelength range of 3.75-3.768 μm. The same spectra are plotted in a broader wavelength range (3.73-3.87 μm) in Figure 4(b). The inset shows the experimental spectrum plotted in a dB scale, where insertion loss (IL) of 1.1 dB and an extinction ratio of 19 dB are indicated.

pass-band optical filtering. In particular, this effect is generated when the output phase shift between the signals propagating in the upper and lower MZI arms is equal to $m2\pi$, with m an integer number (m = 1, 2,…,). In other words, the flat bands correspond to a stable condition of constructive interference at the output combiner, which is also held within a relatively wide wavelength range (e.g., ~ 10 nm) and generates a pass band ripple smaller than 1 dB.

Fano #A and Fano #B also differ from each other because of the directional coupler interaction length, L_i, which is equal to 5 μm in the latter, thus resulting in different power coupling coefficients compared to Fano #A devices. In fact, Figs. 4(a)-4(e) correspond to directional coupler gaps of 300 nm, 400 nm, 700 nm, 800 nm, and ∞, respectively, and the corresponding estimated power coupling coefficients, κ_c^2, are equal to 0.81, 0.60, 0.18, 0.12, and 0. Finally, these results demonstrate that power coupling coefficients higher than 0.5 (i.e., g upper limit of 700 nm) are also suitable for generating sharp asymmetric Fano resonances in RR-coupled MZIs operating at mid-IR wavelengths.

In Fig. 5, the spectrum of the Fano #B configuration characterized by a directional coupler gap, g = 400 nm, is plotted in the wavelength range of 3.75-3.768 μm, which was selected to be narrower compared to Fig. 4(b) in order to appreciate a sharp asymmetric Fano-type resonance. In particular, the same wavelength-dependent transmittance is plotted in a decibel scale (dB) in the inset of Fig. 5, where an insertion loss of 1.1 dB and an extinction ratio of ~ 19 dB can be seen. It is worth specifying that these performance are comparable to the state-of-the-art (insertion loss of ~ 1 dB [18], extinction ratio of ~20 dB [26]) and even better than other proposed configurations characterized by insertion loss of ~ 8 dB [21]. Furthermore, we estimated the maximum slope of the asymmetric Fano resonance $S_{\mathrm{Fano}} = \Delta T/\Delta\lambda$ equal to -574.61/μm (Fig. 5), where ΔT is the difference of two transmittance values and $\Delta\lambda$ the difference of the corresponding wavelengths. Although this value is lower than state-of-the-art device sensitivities achieved in a different Fano architectures, for example characterized by coupled ring resonators operating at 1.55 μm [23], it is worth specifying that the proposed mid-IR Fano architectures were not optimized for sensing applications and that valuable performance comparisons should be carried out between similar structures. To this purpose, the achieved Fano sensitivity is estimated to be 35.5 % higher than the slope of Lorentzian-type resonances of the single ring resonator, i.e. when it is not loaded on the MZI arm, and characterized by R = 60 μm, L_i = 5 μm, g = 400 nm (κ_c^2 = 0.6). This represents an improvement compared to a demonstrated percentage of 30 % reported in [22] and achieved by a similar device architecture.

According to the estimation of the Fano sensitivity aforementioned, it is worth generalizing this investigation and exploring possible applications of the demonstrated devices. In particular, by following the same notation used in [22], the sensitivity of the Fano architecture to a measurand γ can be written as $S = S_1 \cdot S_2$, where S_1 is equal to S_{Fano} and $S_2 = \Delta\lambda/\Delta\gamma$, thus indicating the changes of the ring resonator resonant wavelengths as a function of the measurand. Actually, possible applications that can be implemented as based on the variation of the ring resonant condition and that can be of interest in the vibrating mid-IR wavelength range are i) optical switching and filtering by using heaters for thermo-optic tuning of ring resonator optical waveguides, ii) refractive index and absorption-based photonic sensing. In fact, specific design strategies should be implemented depending of the required application and, in this perspective, insertion loss of 1.1 dB, extinction ratio of 19 dB, flat-band span with a pass band ripple less than 1 dB and a slope of -574.61/μm are already demonstrated as optimal performance for future high-performance optical filtering and switching applications. Conversely, the proposed Fano architectures should be properly optimized for photonic sensing and design strategies and guidelines are elucidated to this purpose.

Actually, the RR-coupled MZI devices can operate as high-performance mid-IR photonic sensors if the ring resonator loaded on one arm of the MZI is exposed to the sensitive area, i.e., the place where the measurand to detect is concentrated, while the rest of the device is fully covered by an insulating cladding. In this way, a change of the cover refractive index, n_c, will influence the ring resonator waveguide effective index, n_{eff}, and finally the ring resonator resonance wavelengths, λ_{res}, determining a wavelength red shift that is proportional to the amount of γ in the sensitive area. In a first order approximation, a compact formula for the resonance wavelength shift in a ring resonator can be written as $\Delta\lambda_{res} = (\Delta n_{eff} \cdot \lambda_{res})/n_g$, where n_g is the waveguide group index and $\Delta n_{eff} = \Delta n_c \cdot (\partial n_{eff}/\partial n_c)_{\lambda_{res}, n_c^0} = \Delta n_c S_{wg}$, with n_c^0 being the cover refractive index when there is no measurand into the sensitive area. Finally, S_{wg} is the waveguide sensitivity [40]. By referring to Fig. 5, a cover refractive index change determines the asymmetric Fano resonance to be shifted to longer wavelengths with respect to the initial condition [33]. Actually, a wavelength sensitivity, $S_2 = S_\lambda = \Delta\lambda_{res}/\Delta n_c$, is defined and can be measured in μm/RIU (refractive index unit). By interrogating the sensor with a fixed wavelength emitted by a laser source at the operating point corresponding to the maximum slope of the Fano resonance, a short wavelength shift can determine a dramatic variation of the optical signal amplitude, ΔT, at the readout. Specifically, the analytic expression for the amplitude variation can be derived as $\Delta T = (S_{Fano} S_{wg} \Delta n_c \lambda_{res})/n_g$, meaning that the amplitude variation at the readout is directly proportional to the slope of the asymmetric Fano resonance $S_1 = S_{Fano}$ and the sensitivity of the ring resonator waveguide structure S_2, with $S = S_1 \cdot S_2$. Finally, the rib waveguides operating in TE mode and used in this investigation, are characterized by a low homogeneous sensitivity ($S_{wg} \cong 0.1$) as the proposed

devices were not optimized for photonic sensing. To this purpose, it is worth noting that mid-IR rib waveguide operating in TM (i.e., transverse magnetic) mode would enhance the sensitivity due to a better overlap between the optical mode and the upper cladding, where the measurand to detect is concentrated. However, a silicon layer thicker than 400 nm is required for TM rib waveguides, thus resulting in a technology platform that is no longer standard for both near-IR and mid-IR silicon photonic device fabrication. In this context, low-loss mid-IR slot waveguides, which have been already demonstrated by the authors at 3.8 μm using the standard silicon-on-insulator technology platform with a 400 nm-thick silicon layer, would allow to achieve the maximum sensitivity of $S_{wg} \cong 1$, and are the best option to maximize the Fano performance in case of photonic sensing application [44].

In conclusion, Fano sensors can assist the operation of sophisticated mid-IR spectrometers where it is useful to simultaneously measure both the optical absorption and refractive index changes [45]. Finally, optimized Fano sensing configurations can exhibit a limit of detection of $\Delta n_c \sim 10^{-4} - 10^{-5}$ RIU and can be used for detecting small refractive index changes, thus providing accurate estimation of detrimental wavelength drifts due, for example, to contaminants in the sensitive area.

4. CONCLUSION

To summarize, we have demonstrated CMOS-compatible photonic integrated devices characterized by RR-coupled MZIs for the generation of the sharp asymmetric Fano resonance at mid-IR wavelengths. Insertion loss and extinction ratio equal to ~ 1 dB and ~ 19 dB, respectively, with a maximum Fano resonance slope of -574.61/μm have been achieved. Specifically, the Fano sensitivity is estimated to be 35.5 % higher than the slope of Lorentzian-type resonances of the single ring resonator when it is not loaded on the MZI arm.

In fact, Fano #B devices with directional coupler interaction length $L_i \neq 0$ can offer design and fabrication approaches that are more tolerant against process variability compared to Fano #A configurations characterized by a point coupling ($L_i = 0$) between the ring resonator and MZI. Furthermore, a detailed experimental investigation of the influence of the power coupling coefficients on the Fano transmittances has been reported, demonstrating a good agreement with simulation results. In particular, threshold values of the directional coupler gap suitable for achieving strong coupling efficiency and asymmetric Fano resonances have been determined in both Fano #A and Fano #B configurations. As a result, gap values should be smaller than 700 nm in both architectures, corresponding to power coupling coefficients $\kappa_c^2 > 0.1$ and $\kappa_c^2 > 0.18$ in Fano #A and Fano #B, respectively. In addition, the free spectral range of the MZI should be larger than double the ring resonator free spectral range to exhibit Fano resonances and typical broadband flat-band spans with a pass band ripple less than 1 dB.

In conclusion, it is worth specifying that the performances achieved are considered to be suitable for realizing efficient mid-IR tunable optical filters by means of heaters on ring resonator optical waveguides. Furthermore, design guidelines and optimization strategies for realizing high-performance refractive index sensing have been elucidated in detail. In particular, a limit of detection of $10^{-4} - 10^{-5}$ RIU has been estimated and application in next generation mid-IR integrated spectrometers is also suggested.

Future work will focus on the experimental demonstration of filtering applications as well as photonic sensing functionalities by means of optimized mid-IR Fano devices.

Funding. MIGRATION (EP/L01162X/1); MERMIG (grant n. 313037).

Acknowledgment. G. Z. Mashanovich would like to acknowledge support from the Royal Society through his University Research fellowship.

REFERENCES

1. M. Sieger, and B. Mizaikoff, "Toward on-chip mid-infrared sensors," Anal. Chem. **88**, 5562-5573 (2016).
2. R. Wang, A. Vasiliev, M. Muneeb, A. Malik, S. Sprengel, G. Boehm, M.-C. Amann, I. Šimonytė, A. Vizbaras, K. Vizbaras, R. Baets, and G. Roelkens, "III-V-on-silicon photonic integrated circuits for spectroscopic sensing in the 2-4 μm wavelength range," Sensors **17**, 1788 (2017).
3. A. Spott, E. J. Stanton, N. Volet, J. D. Peters, J. R. Meyer, and J. E. Bowers, "Heterogeneous integration for mid-infrared silicon photonics," IEEE J. Sel. Top. Quantum Electron. **23**, 8200810 (2017).
4. T. Hu, B. Dong, X. Luo, T.-Y. Liow, J. Song, C. Lee, and G.-Q. Lo, "Silicon photonic platforms for mid-infrared applications [invited]," Photonics Res. **5**, 417-430 (2017).
5. G. Z. Mashanovich, F. Y. Gardes, D. J. Thomson, Y. Hu, K. Li, M. Nedeljkovic, J. Soler Penadés, A. Z. Khokhar, C. J. Mitchell, S. Stankovic, R. Topley, S. A. Reynolds, Y. Wang, B. Troia, V. M. N. Passaro, C. G. Littlejohns, T. Dominguez Bucio, P. R. Wilson, and G. T. Reed, "Silicon photonic waveguides and devices for near- and mid-IR applications," IEEE J. Sel. Top. Quantum Electron. **21**, 8200112 (2015).
6. G. Z. Mashanovich, C. J. Mitchell, J. Soler Penadés, A. Z. Khokhar, C. G. Littlejohns, W. Cao, Z. Qu, S. Stanković, F. Y. Gardes, T. B. Masaud, H. M. H. Chong, V. Mittal, G. S. Murugan, J. S. Wilkinson, A. C. Peacock, and M. Nedeljkovic, "Germanium mid-infrared photonic devices," J. of Lightw. Technol. **35**, 624-630 (2017).
7. B. Troia, A. Z. Khokhar, M. Nedeljkovic, J. Soler Penadés, V. M. N. Passaro, and G. Z. Mashanovich, "Cascade-coupled racetrack resonators based on the Vernier effect in the mid-infrared," Opt. Express **22**, 23990-24003 (2014).
8. B. Troia, J. Soler Penadés, A. Z. Khokhar, M. Nedeljkovic, C. Alonso-Ramos, V. M. N. Passaro, and G. Z. Mashanovich, "Germanium-on-silicon Vernier-effect photonic microcavities for the mid-infrared," Opt. Lett. **41**, 610-613 (2016).
9. L. Carletti, M. Sinobad, P. Ma, Y. Yu, D. Allioux, R. Orobtchouk, M. Brun, S. Ortiz, P. Labeye, J. M. Hartmann, S. Nicoletti, S. Madden, B. Luther-Davies, D. J. Moss, C. Monat, and C. Grillet "Mid-infrared nonlinear optical response of Si-Ge waveguides with ultra-short optical pulses", Opt. Express **23**, 32202-32214 (2015).
10. J. M. Ramirez, V. Vakarin, C. Gilles, J. Frigerio, A. Ballabio, P. Chaisakul, X. Le Roux, C. Alonso-Ramos, G. Maisons, L. Vivien, M. Carras, G. Isella, and D. Marris-Morini "Low-loss Ge-rich Si 0.2 Ge 0.8 waveguides for mid-infrared photonics", Opt. Lett. **42**, 105-108 (2017).
11. J. M. Ramirez, V. Vakarin, J. Frigerio, P. Chaisakul, D. Chrastina, X. Le Roux, A. Ballabio, L. Vivien, G. Isella, and D. Marris-Morini, "Ge-rich graded-index $Si_{1-x}Ge_x$ waveguides with broadband tight mode confinement and flat anomalous dispersion for nonlinear mid-infrared photonics", Opt. Express **25**, 6561-6567 (2017).
12. A. Malik, M. Muneeb, S. Pathak, Y. Shimura, J. Van Campenhout, R. Loo, and G. Roelkens, "Germanium-on-silicon mid-infrared arrayed waveguide grating multiplexers," IEEE Photon. Tech. Lett. **25**, 1805-1808 (2013).
13. T.-H. Xiao, Z. Zhao, W. Zhou, M. Takenaka, H. K. Tsang, Z. Cheng, and K. Goda, "Mid-infrared germanium photonic crystal cavity," Opt. Lett. **42**, 2882-2885 (2017).
14. U. Fano, "Effects of configuration interaction on intensities and phase shifts," Phys. Rev. **124**, 1866-1878 (1961).
15. A. E. Miroshnichenko, S. Flach, and Y. S. Kivshar, "Fano resonances in nanoscale structures," Rev. Mod. Phys. **82**, 2257-2298 (2010).
16. M. F. Limonov, M. V. Rybin, A. N. Poddubny, and Y. S. Kivshar, "Fano resonances in photonics," Nat. Photonics **11**, 543-554 (2017).

17. B. Luk'yanchuk, N. I. Zheludev, S. A. Maier, N. J. Halas, P. Nordlander, H. Giessen, and C. T. Chong, "The Fano resonance in plasmonic nanostructures and metamaterials," Nat. Mater. **9**, 707-715 (2010).
18. S. Darmawan, Y. M. Landobasa, P. Dumon, R. Baets, and M. K. Chin, "Nested-ring Mach-Zehnder interferometer in silicon-on-insulator," IEEE Photon. Technol. Lett. **20**, 9-11 (2008).
19. G. Zhao, T. Zhao, H. Xiao, Z. Liu, G. Liu, J. Yang, Z. Ren, J. Bai, and Y. Tian, "Tunable Fano resonances based on microring resonator with feedback coupled waveguide," Opt. Express **24,** 20187-20195 (2016).
20. X.-Y. Zhang, T. Zhang, X.-J. Xue, J.-L. Zhang, J. Hong, P.-Q. Wu, and Q.-Y. Chen, "Tunable optical ring resonator integrated with asymmetric Mach-Zehnder interferometer," IEEE J. of Lightw. Technol. **28**, 2512-2520 (2010).
21. J. Song, Q. Fang, S. H. Tao, M. B. Yu, G. Q. Lo, and D. L. Kwong, "Passive ring-assisted Mach-Zehnder interleaver on silicon-on-insulator," Opt. Express **16**, 8359-8365 (2008).
22. M. Terrel, M. J. F. Digonnet, and S. Fan, "Ring-coupled Mach-Zehnder interferometer optimized for sensing," Appl. Opt. **48**, 4874-4879 (2009).
23. X. Zhou, L. Zhang, A. M. Armani, J. Liu, X. Duan, D. Zhang, H. Zhang, and W. Pang, "An integrated photonic gas sensor enhanced by optimized Fano effects in coupled microring resonators with an athermal waveguide," IEEE J. of Lightw. Technol. **33**, 4521-4530 (2015).
24. D. Irawan, T. Saktiotio, J. Ali, and P. Yupapin, "Design of Mach-Zehnder interferometer and ring resonator for biochemical sensing," Photonic Sensors **5**, 12-18 (2015).
25. Y. Zhang, S. Darmawan, L. Y. M. Tobing, T. Mei, and D. H. Zhang, Coupled resonator-induced transparency in ring-bus-ring Mach-Zehnder interferometer," J. Opt. Soc. Am. B **28**, 28-36 (2011).
26. T. Hu, P. Yu, C. Qiu, H. Qiu, F. Wang, M. Yang, X. Jang, H. Yu, and J. Yang, "Tunable Fano resonances based on two-beam interference in microring resonator," App. Phys. Lett. **102**, 011112-1 - 011112-4 (2013).
27. L.-W. Luo, S. Ibrahim, A. Nitkowski, Z. Ding, C. B. Poitras, S. J. Ben Yoo, and M. Lipson, "High bandwidth on-chip silicon photonic interleaver," Opt. Express **18**, 23079-23087 (2010).
28. L. Y. M. Tobing, L. Tjahjana, S. Darmawan, and D. H. Zhang, "Numerical and experimental studies of coupling-induced phase shift in resonator and interferometric integrated optics devices," Opt. Express **20**, 5789-5801 (2012).
29. G. Wang, T. Dai, J. Jiang, H. Yu, Y. Hao, Y. Wang, Y. Li, X. Jiang, and J. Yang, "Slope tunable Fano resonances in asymmetric embedded microring resonators," J. Opt. **19**, 025803 (2017).
30. S. Longhi, "Tunable dynamic Fano resonances in coupled-resonator optical waveguides," Phys. Rev. A **91**, 063809 (2015).
31. Y. Lu, J. Yao, X. Li, and P. Wang, "Tunable asymmetrical Fano resonance and bistability in a microcavity-resonator-coupled Mach-Zehnder interferometer," Opt. Lett. **30**, 3069-3071 (2005).
32. G. Wang, A. Shen, C. Zhao, L. Yang, T. Dai, Y. Wang, Y. Li, X. Jang, and J. Yang, "Fano-resonance-based ultra-high-resolution ratio-metric wavelength monitor on silicon," Opt. Lett. **41**, 544-547 (2016).
33. Y. Tang, Z. Zhang, R. Wang, Z. Hai, C. Xue, W. Zhang, and S. Yan, "Refractive index sensor based on Fano resonances in metal-insulator-metal waveguides coupled with resonators," Sensors **17**, E784 (2017).
34. Y. Shuai, D. Zhao, G. Medhi, R. Peale, Z. Ma, W. Buchwald, R. Soref, and W. Zhous, "Fano-resonance photonic crystal membrane reflectors at mid- and far-infrared," IEEE Photon. J. **5**, 4700206 (2013).
35. N. Nguyen-Huu, M. Cada, Y. Ma, F. Che, J. Pistora, K. Yasumoto, Y. Ma, J. Lin, and H. Maeda, "Mid-infrared Fano resonance in heavily dopes silicon and metallic nanostructures due to coupling of Wood-Rayleigh anomaly and surface plasmons," J. Phys. D: Appl. Phys. **50**, 205105 (2017).
36. J. Guo, L. Jiang, X. Dai, and Y. Xiang, "Tunable Fano resonances of a graphene/waveguide hybrid structure at mid-infrared wavelength," Opt. Express **25**, 4740-4748 (2016).
37. E. Lee, I. C. Seo, S. C. Lim, H. Y. Jeong, and Y. C. Jun, "Active switching and tuning of sharp Fano resonances in the mid-infrared spectral region," Opt. Express **24**, 25684-25696 (2016).
38. A. Vasiliev, A. Malik, M. Muneeb, R. Baets, and G. Roelkens, "Photothermal mid-infrared spectroscopy using Fano resonances in silicon microring resonators," in conference on lasers and electro-optics (CLEO): science and innovation 2016, San Jose, California US, 5-10 June 2016, paper SF2H.5, ISBN: 978-1-943580-11-8.
39. M. Nedeljkovic, A. Z. Khokhar, Y. Hu, X. Chen, J. Soler Penades, S. Stankovic, H. M. H. Chong, D. J. Thomson, F. Y. Gardes, G. T. Reed, and G. Z. Mashanovich, "Silicon photonic devices and platforms for the mid-infrared," Opt. Mat. Express **3**, 1205-1214 (2013).
40. W. Bogaerts, P. De Heyn, T. Van Vaerenbergh, K. De Vos, S. K. Selvaraja, T. Claes, P. Dumon, P. Bienstman, D. Van Thourhout, and R. Baets, "Silicon microring resonators," Laser Photon. Rev. **6**, 47-73 (2012).
41. R. A. Soref, S. J. Emelett, and W. R. Buchwald, "Silicon waveguided components for the long-wave infrared region", J. Opt. A: Pure Appl. Opt. **8**, 840-848 (2006).
42. B. Troia, F. De Leonardis, and V. M. N. Passaro, "Generalized modelling for the design of guided-wave optical directional couplers," Opt. Lett. **39**, 1161-1164 (2014).
43. G. Z. Mashanovich, M. M. Miloševic, M. Nedeljkovic, N. Owens, B. Xiong, E. J. Teo, and Y. Hu, "Low loss silicon waveguides for the mid-infrared," Opt. Express **19**, 7112-7119 (2011).
44. J. S. Penadés, A. Z. Khokhar, M. Nedeljkovic, and G. Z. Mashanovich, "Low-loss mid-infrared SOI slot waveguides," IEEE Photon. Tech. Lett. **27**, 1197-1199 (2015).
45. V. M. N. Passaro, B. Troia, F. De Leonardis, "A generalized approach for design of photonic gas sensors based on Vernier-effect in mid-IR," Sens. Actuators B Chem. **168**, 402-420 (2012).